NOTE

Magnetic Resonance in Medicine 00:00–00 (2015)

3D-Printed Shepp-Logan Phantom as a Real-World Benchmark for MRI

Jeffrey A. Kasten,* Thomas Vetterli, François Lazeyras, and Dimitri Van De Ville

Purpose: As prescribed and reliable geometrical entities, phantoms have served as indispensable validation tools in a variety of MR-related topics. Though a number of phantoms have been conceived, certain applications may warrant highly customized geometries. The purpose of this study was to demonstrate the expediency of rapid prototyping for generating a flexible class of MR-compatible phantom designs.

Methods: An incarnation of the three-dimensional Shepp-Logan numerical phantom, amended for use in magnetic resonance spectroscopic imaging, was actualized using rapid prototyping. Each of the comprising compartments was filled with a solution containing prepared concentrations of common ^{1}H brain metabolites. Analytical Fourier expressions for the phantom class were established in order to generate a set of simulated measurements, which were then contrasted with acquired data.

Results: Experimental results for both structural and spectroscopic imaging substantiate the suitability of rapid prototyping for MR phantom applications. The analytically simulated measurements show excellent agreement with the measured data, but also highlight the various consequences effectuated when certain aspects of the acquisition model are disregarded or misrepresented.

Conclusion: Rapid prototyping offers a novel and versatile framework for MR phantom-based validation studies. Furthermore, the growing accessibility and open-source compatibility may provide an important link between the often disparate numerical and haptic testing. **Magn Reson Med 000:000–000, 2015.** © **2015 Wiley Periodicals, Inc.**

Key words: phantom; Shepp-Logan; 3D printing; analytical Fourier transform; magnetic resonance spectroscopic imaging; reconstruction

INTRODUCTION

A prevailing means for any type of MR validation is through the use of phantoms, i.e., objects of known geometry and/or composition, that serve to reduce the number of experimental confounds. These phantoms can either be haptic, as is common when calibrating scanner hardware or designing pulse sequences, or numeric, whereby the target object is digitally generated. The latter type of phantom is often used to simulate MR measurements in lieu of real data when access to a scanner is restricted or cost-prohibitive. Numerical phantoms are especially prevalent in the image processing and image reconstruction fields, as they facilitate quantitative comparison between different algorithms and enable optimization over a wide variety of applicable image/object classes. Nonetheless, when presented with real measurements, the efficacy of many MR reconstruction algorithms is circumscribed by the degree to which they accurately represent the acquisition process (hereafter referred to as the "forward model"). Hence, an ideal test bed would be one where a physical phantom were available in conjunction with its numeric counterpart, enabling a more realistic performance assessment as an end measure.

Although there are several phantoms on the market, they are often quite costly and may only partially fulfill the requirements of a particular application. Such is certainly the case for MR spectroscopic imaging (MRSI), which has traditionally appropriated phantoms designed primarily for single-voxel spectroscopic (SVS) assessments. Although it is possible to commission or develop customized phantoms in accordance with specific requirements, the time required for prototyping and fabrication, as well as the associated costs, remain limiting factors.

One possible avenue for simultaneously addressing these issues is rapid prototyping, better known as three-dimensional (3D) printing or additive manufacturing. Here, computer-assisted design (CAD) software is used to generate models represented by faceted meshes, which are then exported to a printer that gradually produces a solid object by successively layering material. Although additive manufacturing technology has existed for nearly 30 years (1), it has recently experienced an explosion in popularity due to the increased accessibility of consumer-level printers, mostly under the fused deposition modeling platform, which uses extruded thermoplastics to fabricate each layer. Furthermore, most interfacing software for 3D printers requires only a stereolithography file, promoting and facilitating the open-source exchange of designs and culminating in numerous online repositories. 3D printing is therefore an attractive prospect for MR applications due to the falling costs, routine use of MR-compatible materials such as acrylonitrile butadiene styrene (ABS), and congruence of feasible designs with a class of analytical Fourier transforms.

Given the above conditions, 3D printing has the potential to precipitate a wealth of innovative, open-source phantom designs in addition to other MR applications. As an overview, we provide a brief survey of current trends in both haptic and numerical MR phantom design.

École Polytechnique Fédérale de Lausanne, Institute of Bioengineering, Lausanne, Switzerland

Grant sponsor: Center for Biomedical Imaging; Grant sponsor: Swiss National Science Foundation; Grant number: SNF 3200300-135425.

*Correspondence to: Jeffrey A. Kasten, B.A., École Polytechnique Fédérale de Lausanne, Institute of Bioengineering, EPFL-STI-IBI, Bâtiment BM 4.130, Lausanne, Vaud CH-1015, Switzerland. E-mail: jeffrey.kasten@epfl.ch

Received 13 August 2014; revised 2 December 2014; accepted 3 December 2014

DOI 10.1002/mrm.25593

Published online 00 Month 2015 in Wiley Online Library (wileyonlinelibrary.com).

Phantom Design

The salient objective is to ensure that a given phantom design enables straightforward investigation of the target processes or phenomena, hence most phantoms are devised with particular applications in mind. For example, apart from the standard test phantoms provided by the major scanner vendors, specialized phantoms, such as the ACR (2) and ADNI (3) phantoms, have been created for testing signal-to-noise ratio, contrast-to-noise ratio, geometrical uniformity, slice thickness accuracy, and so forth in order to synchronize and/or normalize scan parameters across vendors and institutions in large multisite studies. Wang et al. (4) constructed a 3D grid phantom in order to measure and compensate for image distortions due to gradient nonlinearities. Moreover, the merits of 3D printing have recently been demonstrated for such applications; for example, O'Callaghan et al. (5) customized a 3D-printed grid array to the bore dimensions of a preclinical 9.4T scanner for gradient system calibration. With regard to MR spectroscopy and MRSI, phantoms designed as benchmarks for spectral measurements have mainly been restricted to simple geometries such as a single sphere filled with a solution comprised of metabolites of interest, which have a limited capacity for assessing spatial characteristics. In contrast, Woo et al. (6) created a phantom consisting of an array of cone-shaped vials filled with various metabolites, whereby the solution volume in a given MRSI slice could be modulated by changing the slice position.

On the numerical side, it is often common practice to evaluate a given reconstruction method based on rasterized images/volumes. Nonetheless, care must be taken when using these models to simulate measured data, particularly during the forward Fourier transform step, as the continuous-discrete nature of the process is misrepresented. A much-preferred scenario is when an analytical expression for the continuous-domain Fourier transform of the desired object is available, allowing simulations that are devoid of discretization errors and independent of resolution. Though analytical Fourier expressions for arbitrary geometries may be difficult or even impossible to obtain, a number of works have presented analytical solutions for certain object classes. One of the initial works pertains to the inception of the now ubiquitous Shepp-Logan phantom (7), proposing an analytical expression for the Fourier transform of an object comprised of two-dimensional (2D) ellipses, which was later extended to 3D (8). These object classes have been supplemented by the inclusion of Gaussian functions (9), linearly varying functions with polygonal support (10), and 3D polyhedra, (11,12). Recently, Guerquin-Kern et al. (13) extended these polygonal regions to those defined by 2D spline or Bézier contours, and even allowed for the modulation by sinusoidal or polynomial functions to mimic sensitivity maps for parallel MRI.

Although a diverse assortment of functions may be approximated by the above geometrical classes, translating a given design to a physically realizable model may still prove to be a formidable or costly process. Furthermore, extending the analytical Fourier expressions associated with these classes to those representing a finite slice thickness may not be straightforward, thus precluding the ability to accurately model partial volume effects. As such, 3D printing offers a compelling resolution, significantly expediting the fabrication process, and proffering a set of CAD-driven faceted geometrical models where analytical Fourier transforms are available for representing both the full 3D object and its 2D projections.

We next describe the design and fabrication of a novel 3D-printed phantom for use in MRSI measurements, and present both experimental data and simulated measurements. In the spirit of open science, we have made all designs, as well as all software for visualization and calculation of simulated k-space data publicly available for maximal reproducibility (http://miplab.epfl.ch/software/MRphantom).

METHODS

3D Shepp-Logan MRSI Phantom

Motivated by the paucity of structurally heterogeneous phantoms suitable for MRSI measurements, we decided to begin our investigations by designing a 3D variant of the Shepp-Logan phantom, prescribing for each compartment a solution of known spectral content. The Shepp-Logan phantom was selected as a reference due to its simplicity, yet appositeness in representing prominent anatomical features of the human head, as well as its omnipresence among the image processing community. Certain adaptations, however, were necessary in order for the design to remain compatible with both the 3D printing process and the aims of the MRSI experiment. These mandated a tapering of the ellipsoids to ensure adequate structural support at each stage of printing, and a means of filling the ellipsoids with the desired solutions. The smallest ellipsoids (corresponding to regions *h*, *i*, and *j* in the original Shepp-Logan manuscript) were also restricted to remain spherical, and were scaled such that the diameter of each was comparable to the nominal voxel sizes in common MRSI settings. A schematic drawing of the finalized design is provided in Figure 1. The material thickness of each of the interior compartments was chosen to be 2 mm, whereas the outer concentric shells were given a 3-mm thickness. The base plate thickness was set at 5 mm with a 9-mm wall height. These values were shown to represent a good compromise between the required structural integrity, material usage, and the risk of component permeability. All designs were conceived using Sketchup Make 8 (Trimble Navigation Limited, Sunnyvale, California, USA).

The model was then exported as a stereolithography file and printed on a Stratasys Fortus 250mc (Stratasys Ltd., Eden Prairie, Minnesota, USA/Rehovot, Israel) using ABS, for which select material properties are provided in Supporting Table S1. ABS is an attractive choice for MR applications due to its low magnetic susceptibility, effectively rendering ABS structures as "MR-invisible." The minimum achievable layer thickness for the printer (used for this study) is 0.178 mm, with a nominal achievable in-plane accuracy of ± 0.241 mm (manufacturer specifications). During the fabrication process, the model geometry dictated that each of the components be printed separately. This is due to the fact

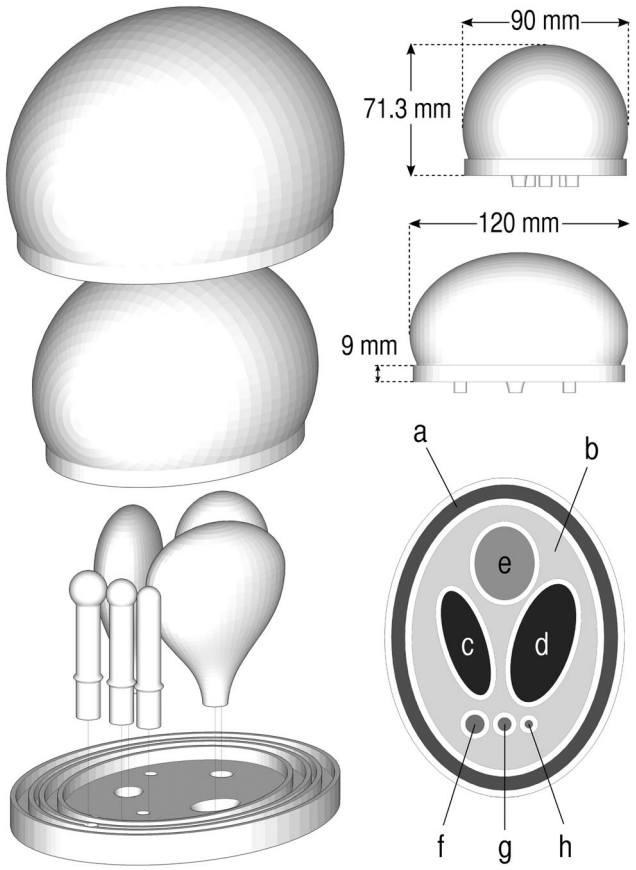

FIG. 1. Schematic diagram of the 3D-printed Shepp-Logan phantom. Left: Perspective view of the individual components comprising the phantom. Top right: Profile views of the assembled phantom. Bottom right: Axial section portraying the various phantom regions. Grayscale intensities serve as an aid to distinguish between spectrally-homogeneous compartments.

that the printer can only achieve a reliable layering when there is adequate support underneath. Practically, most systems mandate that the angle formed between the surface normals and the printing plane, θ, be such that $\theta \in [-45^{\circ}, 225^{\circ}]$. When θ falls outside of this range, an ancillary water-soluble material is printed to provide temporary support, which is removed after printing. The entire phantom required approximately 10 hours of fabrication time, leading to a total manufacturing cost of around $300 US. Once printed, the fidelity of the phantom to the original design was verified using a set of digital calipers.

Although the completed parts should represent "solid" objects, several factors may preclude complete impermeability, such as incomplete layer adhesion or compromises in the trajectory of the extruder. This can present a problem if contamination between compartment-specific solutions is to be avoided. We therefore coated the exterior (and when possible, interior) surface of each printed component with a two-part waterproof epoxy resin (*Prestolith special epoxy resin*; MOTIP DUBPLI GmbH, Haßmersheim, Germany), which has a nominal mixed viscosity of 950 mPa/s (per the manufacturer's specifications). The same epoxy was used to join the separate components and to attach Luer connectors to the filling inlets leading into compartments *a* and *b* (Fig. 1), which culminated in a robust object once assembled. The various stages of the phantom construction are documented in Figure 2. Note that given the asymmetry of the protruding inlets, the phantom can be unambiguously oriented within the MR scanner.

Upon assembly, interior phantom compartments *b*, *e*, *f*, *g*, and *h* were filled with solutions consisting of various concentrations of common brain metabolites, namely, *N*-acetyl-L-aspartic acid, choline chloride, creatine, and sodium L-lactate (all from Sigma-Aldrich, St. Louis, Missouri, USA), prepared in phosphate-buffered saline (Thermo Fisher Scientific, Waltham, Massachusetts, USA) containing 0.02% sodium azide to preclude microbial contamination. The pH of each solution was adjusted to 7.2. Compartments *c* and *d* consisted of just the buffer solution. The outer compartment (*a*) was filled with corn oil (Sigma-Aldrich) to mimic extracranial lipids. Specific concentrations and calculated volumes for all compartments are provided in Table 1. No additional T_1-shortening agents were used. The utilized concentrations were chosen as significantly higher than those normally encountered in vivo in order to achieve a signal-to-noise ratio that was better suited for testing and validation. When filling each of the compartments, special care was taken to inhibit air bubble formation, which can engender severe susceptibility artifacts in the acquired images. For the main compartment (*b*), the two filling inlet connections were used to mount a series of Luer valves, allowing a closed fluid flow loop to be formed and any large air bubbles to be isolated and subsequently evacuated. For the remaining compartments, extra-long syringe needles were used to ensure that solution filling began at the base of each compartment. Once filled, compartments *a* and *b* were sealed using threaded

FIG. 2. Top left: Printed phantom components. Top right: Completed phantom. Bottom: Partially assembled phantom following application of epoxy coating.

Table 1
Volumes, Solution Contents, and Concentrations for Each of the Phantom Compartments

Region	Volume, mL	*N*-acetyl-L-aspartic acid, mM	Creatine, mM	Choline chloride, mM	Sodium L-lactate, mM	Corn oil
a	90.543	—	—	—	—	0.9 g/mL at 25°C
b	165.233	50	25	—	—	—
c	11.372	—	—	—	—	—
d	19.547	—	—	—	—	—
e	9.175	—	—	50	50	—
f	0.432	50	50	10	—	—
g	0.321	50	50	10	—	—
h	0.278	50	50	10	—	—

All solutions were prepared in phosphate-buffered saline containing 0.02% sodium azide.

stoppers compatible with the Luer connectors; the remaining compartments were sealed using paraffin.

Analytical Computations

General formulations of the analytical Fourier expressions for homogeneous regions with polygonal/polyhedral support can be found in reports by McInturff and Simon (10) and Komrska (12,14). The latter may be used along with a general 3D-faceted model, which can be represented as a superposition of weighted polyhedral regions. Also of interest is the case when a portion of the geometry is to be projected onto the slice plane, as is the case when considering finite slice thicknesses. Without loss of generality, we assume in the following rectangular slices taken along the *z*-axis. Consider a set S describing the slice profile, and $\mathcal{P}$ the family of polyhedral regions comprising the 3D model. The Fourier transform can be expressed as:

$$s(k_x,k_y)=\sum_{n=1}^{|\mathcal{R}|} w_n \iiint_{R^{(n)}\in\mathcal{R}} \rho_n(\boldsymbol{r}) e^{-2\pi j(k_x x+k_y y)}\,dxdydz, \qquad [1]$$

where for $P^{(n)}\in\mathcal{P}$, $\mathcal{R}\ni R^{(n)}\triangleq P^{(n)}\cap S$, $|\cdot|$ denotes set cardinality, $w_n\in\mathbb{R}$, and

$$\rho_n(\boldsymbol{r})=\begin{cases}1, & \boldsymbol{r}\in P^{(n)}\\ 0, & otherwise\end{cases}. \qquad [2]$$

Because each region $R^{(n)}$ consists of planar facets, the integration along z is simply the unsigned area under each face. Defining $\mathcal{F}^{(n)}$ as the family of faces comprising region $R^{(n)}$,

$$\int_{R^{(n)}} \rho_n(\boldsymbol{r})dz=\sum_{i=1}^{|\mathcal{F}_\perp^{(n)}|}\boldsymbol{a}_i^{(n)}\cdot\left(\boldsymbol{r}_\perp-\boldsymbol{r}_{0,i}^{(n)}\right)\chi_i(\boldsymbol{r}_\perp), \qquad [3]$$

where $(\cdot)_\perp$ denotes a projection onto the slice plane. Here, $\boldsymbol{r}_{0,i}^{(n)}$ is an arbitrary point in the plane defined by the i^{th} face, $F_i^{(n)}\in\mathcal{F}^{(n)}$, and

$$\chi_i(\boldsymbol{r}_\perp)=\begin{cases}1, & \boldsymbol{r}_\perp\in F_{i\perp}^{(n)}\\ 0, & otherwise\end{cases}. \qquad [4]$$

The vector $\boldsymbol{a}_i^{(n)}$ can be calculated from the unit normal vector corresponding to $F_i^{(n)}$, $\hat{\boldsymbol{n}}_i^{(n)}=\left(n_{i,x}^{(n)},n_{i,y}^{(n)},n_{i,z}^{(n)}\right)^T$, as $\boldsymbol{a}_i^{(n)}=-\left(n_{i,x}^{(n)}/n_{i,z}^{(n)},n_{i,y}^{(n)}/n_{i,z}^{(n)},1\right)^T$. The full expression is then given by:

$$s(k_x,k_y)=\sum_{n=1}^{|\mathcal{R}|} w_n \sum_{i=1}^{|\mathcal{F}_\perp^{(n)}|}\iint_{F_{i\perp}^{(n)}\in\mathcal{F}^{(n)}}\boldsymbol{a}_i^{(n)}\cdot\left(\boldsymbol{r}_\perp-\boldsymbol{r}_{0,i}^{(n)}\right) e^{-2\pi j\left(k_x x+k_y y\right)}dxdy, \qquad [5]$$

where the integral is fully treated as described by McInturff and Simon (10).

The extension of the above framework to MRSI or other 4D measurements is straightforward so long as the spatial and temporal spaces remain separable, which may be presumed in the absence of spatially-dependent phase perturbations of the temporal signal. In this case, Equation [5] may be adapted as

$$s(k_x,k_y,t)=\sum_{n=1}^{|\mathcal{R}|} w_n\left(\sum_{l=1}^{L}\int_{-\infty}^{\infty}\nu_l^{(n)}(f)e^{-2\pi jft}df\right)\left(\sum_{i=1}^{|\mathcal{F}_\perp^{(n)}|}\iint_{F_{i\perp}^{(n)}\in\mathcal{F}^{(n)}}\boldsymbol{a}_i^{(n)}\cdot\left(\boldsymbol{r}_\perp-\boldsymbol{r}_{0,i}^{(n)}\right)e^{-2\pi j\left(k_x x+k_y y\right)}dxdy\right). \qquad [6]$$

Here, ν_l represents a general spectral line shape function with known analytical Fourier transform. Two common choices are Lorentzian and Gaussian functions:

$$\nu_l^{Lorentz}(f)=\frac{1}{\pi}\frac{(\Gamma_l/2)}{(f-f_l)^2+(\Gamma_l/2)^2}\overset{\mathcal{FT}}{\leftrightarrow}e^{-2\pi jf_l t}e^{-\pi\Gamma_l|t|}, \qquad [7]$$

$$\nu_l^{Gauss}(f)=e^{-\frac{(f-f_l)^2}{2\sigma_l^2}}\overset{\mathcal{FT}}{\leftrightarrow}\sqrt{2\pi\sigma_l^2}e^{-2\pi jf_l t}e^{-2(\pi\sigma_l t)^2}, \qquad [8]$$

respectively.

MR Scanning

All scanning was conducted on a Siemens 3.0T Trio MR scanner (Siemens Healthcare, Erlangen, Germany). The phantom was positioned in the center of a 32-channel phased array head coil, with the major semi-axis oriented along the scanner bore (*z*-direction). First, three coronal slices were acquired with multiple echo times (TEs) using a gradient refocused echo (GRE) sequence such that the position of the top slice roughly

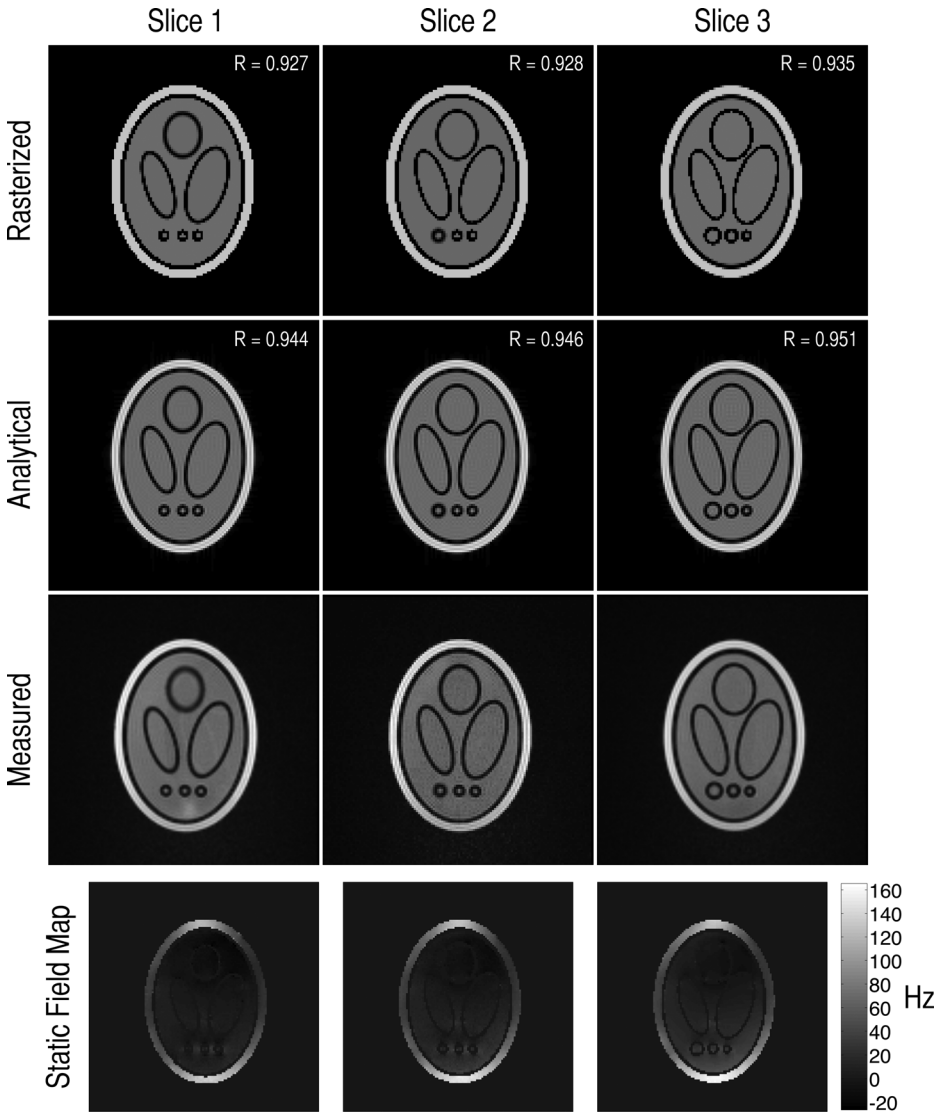

FIG. 3. Reconstructed simulated and acquired images corresponding to each of the GRE measurements. Top row: Rasterized simulated images. Second row: Analytical simulated images. Third row: Measured data. The small hyperintensity in slice 1 can be attributed to a slight miscalibration in the coil-combining algorithm. Bottom row: Static field inhomogeneity profiles for each of the GRE slices. The maximum value of the normalized cross-correlation coefficient (R) between the measured data and both the rasterized and analytical simulations is displayed for each slice and substantiate an increased fidelity of the analytical simulations to the acquired measurements.

corresponded to the center of regions *f*, *g*, and *h* (field of view [FOV] = 160 × 160 × 10 mm, repetition time [TR] = 400 ms, $TE_1 = 2.46$ ms, $TE_2 = 4.92$ ms, flip angle = 60°, bandwidth = 1447 Hz/pixel, nominal voxel size = 1.25 × 1.25 × 3.0 mm, interslice spacing = 3.3 mm). The same spatial positioning and FOV was then used to define a single chemical shift imaging (CSI) slice (TR = 1700 ms, TE = 288 ms, temporal sampling rate = 1.2 kHz, number of temporal samples = 1024, nominal voxel size = 5 × 5 × 10 mm). A transverse, high-resolution 3D MP-RAGE sequence (FOV = 74.38 × 140 × 144 mm, TR = 1750 ms, TE = 2.5 ms, inversion time = 900 ms, flip angle = 9°, bandwidth = 210 Hz/pixel, nominal voxel size = 0.547 × 0.547 × 0.9 mm) was also acquired as a reference for translating the GRE/MRSI slice positioning onto the phantom model. Following phantom scanning, SVS spectra were acquired for each of the prepared solutions using a PRESS sequence (TR = 1700 ms, TE = 288 ms, temporal sampling rate = 2.0 kHz, number of temporal samples = 2048, nominal voxel size = 15 × 15 × 15 mm).

Once suitable position parameters were identified, three slices corresponding to the GRE sequence measurements were generated from the original phantom model, and their analytical Fourier transforms were computed in accordance with Equation [5], with a FOV and nominal spatial resolution chosen to match that of the measured data. The weights, w_n, were selected based on the Bloch equations for the GRE sequence, with literature-derived values of T_1 and T_2 for the buffer solution and corn oil. All calculations were performed in MATLAB 8 (MathWorks, Natick, Massachusetts, USA), on an Intel i7 2.66 GHz processor in Mac OSX 10.8.5 with 8 GB RAM. For comparison, rasterized counterparts for each of the slices were calculated based on MATLAB's native `inpolygon` function, from which k-space data were generated via discrete Fourier transform (DFT). For CSI simulations, spectral parameters for each of the prepared solutions were estimated from the SVS measurements using the HSVD algorithm (15). A CSI slice was then generated from the phantom model as with the GRE data, and analytical k-

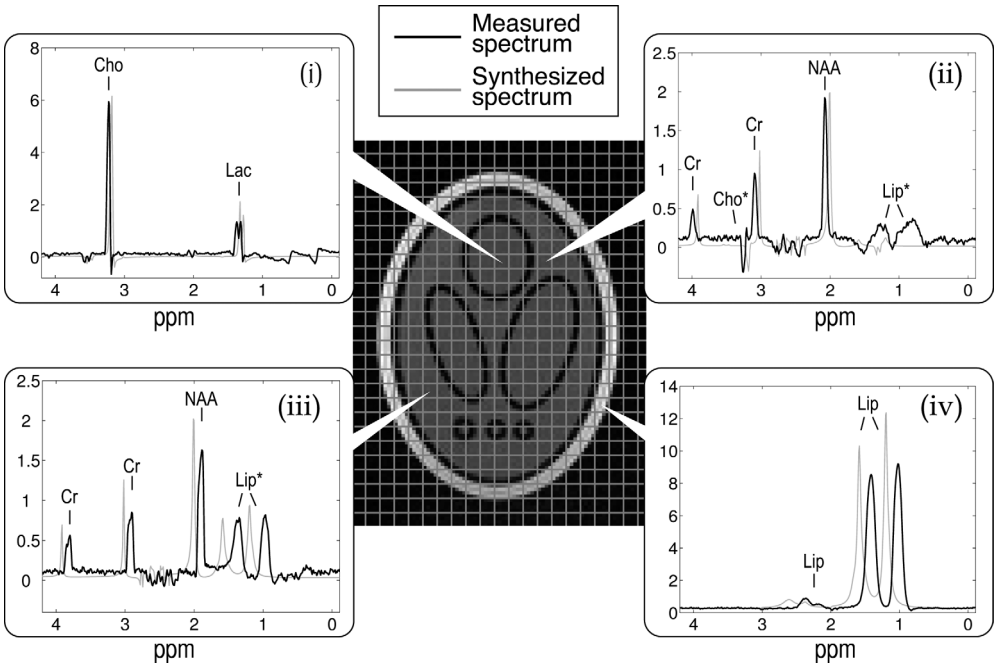

FIG. 4. CSI grid overlaid on a GRE structural image along with sample measured spectra (black), and their analytically simulated counterparts (gray). The latter illuminate the various spectral shifts and line broadening effects due to the static field inhomogeneity present during data acquisition. The usual data truncation artifacts (denoted by an asterisk [*] next to the suspected offending resonance) manifest as spectral leakage of the lipid signals into the interior compartments (i, ii, iii), as well as that of the choline chloride signal in region *e* into region *b* (ii). Vertical axis scaling for all spectral plots is in arbitrary units. Cho, choline chloride; Cr, creatine; Lac, sodium L-lactate; Lip, corn oil; NAA, *N*-acetyl-L-aspartic acid.

space measurements were computed in accordance with Equation [6]. To facilitate visualization and interpretation, the analytical CSI data were then scaled using the choline peak from compartment *e* in the acquired data as a reference, which was selected based on the relatively homogeneous local static inhomogeneity profile.

RESULTS

Corresponding images for each of the rasterized, analytical, and measured datasets are presented in Figure 3; all reconstructions were performed by inverse DFT of the simulated and acquired k-space samples. For the measured data, static field inhomogeneity maps are also shown for each slice, which were generated using the phase of the GRE measurements and then thresholded using the corresponding magnitude images. Maximum normalized cross-correlation coefficients between the measured data and both the rasterized and analytical simulations are also provided for each reconstructed slice. Figure 3 serves as an edifying illustration of various assumptions imposed on the forward model. The utilization of rasterized images (first row) asserts that the object itself is first discretized, and that the acquired measurements are simply its DFT samples. The analytical case (second row) clearly represents a more accurate portrayal of the Fourier transform and down-sampling operations, simultaneously communicating the ramifications of other confounds during the acquisition, as evidenced by a visual comparison with the measured data (third row). Perhaps the most prominent examples are the reduced partial voluming around region *e* in the rasterized and analytical images in slice 1, where an ideal slice-select profile was assumed, and the lack of variation in the RF profile when compared with the measured data. The latter discrepancy may also be elucidated by examining normalized line profile plots for each of the reconstructions, an example of which can be found in Supporting Figure S1. When viewing the static inhomogeneity profiles (fourth row), some susceptibility effects can be recognized, predominantly around the lipid compartment and in the bottom slice around compartments *f*, *g*, and *h*, paralleling the classical field response of a cylinder positioned perpendicular to the primary magnetic field (16).

For the CSI data, a few representative spectra are displayed in Figure 4, where measured spectra are shown superimposed on their simulated counterparts. Here, the usual data truncation artifacts are observed, manifested primarily as spectral leakage of the lipid signals into the interior compartments [Fig. 4(i), 4(ii), and 4(iii)], as well as that of the choline chloride signal in region *e* into region *b* [Fig. 4(ii)]. Spectral shifts and concomitant line broadening effects in the measured data due to the static field inhomogeneity profile can also be discerned.

DISCUSSION

The strong correspondence between the acquired MR measurements and the analytically determined signal, as well as the paucity of any deleterious object-induced artifacts, effectively substantiates the 3D printing framework for MR phantom generation. Furthermore, the CSI measurements do not indicate any sign of solution

contamination between the various compartments, corroborating the efficacy of the fabrication process, although thorough analysis requires additional longitudinal testing. Furthermore, although the acquired static field maps revealed the presence of small susceptibility effects, these may remain inconsequential for a number of applications. Nonetheless, for situations where the elimination of such effects is paramount, the use of fused deposition modeling, which may carry a risk of air becoming trapped between the individual material layers, may be dismissed in favor of alternative rapid prototyping technologies (eg, selective laser sintering) or traditional injection molding. With regard to our specific design, though the overall geometrical structure befitted our experimental aims, some minor modifications may be beneficial when considering future experiments. This would include the incorporation of customized stopper mechanisms into each of the filling inlets, enabling easy inversion of the phantom. Additionally, although the majority of the air bubbles were successfully expelled from the main compartment during the filling stage, some small bubbles remained fixed to the base plate. The identification of these bubbles prior to MR scanning was further obfuscated by the opacity of the printing material, hence future designs may profit from a slight tapering of the base plate in order to help herd tenacious bubbles toward the filling outlets.

It is noteworthy that within the context of MR reconstruction, particular phantom-based validation schemes are typically limited to either haptic or numerical types. However, given the above illustrations, such a dichotomization may ultimately undermine current trends, where alternatives to the standard inverse Fourier transform have arisen either as an attempt to intentionally reduce the number of measurements while maintaining certain standards of image quality [eg, compressed sensing (17), SENSE (18)], or to circumvent the ineluctable artifacts produced by Fourier-based reconstructions, especially when only a limited number of measurements are available. Largely formulated as inverse problems, these approaches have shown promise, yet one factor which may impede their greater acceptance and ultimate assimilation into more widespread practice is that unlike traditional Fourier reconstructions, the attendant artifacts and biases are not well-characterized and understood within the clinical and research communities. Additionally, the source, nature, or appearance of these artifacts may be difficult to gauge in in vivo scenarios, especially when gold standard measurements are unavailable. Although phantom studies serve to mitigate such concerns, exclusive testing may not fully elucidate reconstruction performance in such cases. For example, methods that are optimized based on numerical simulations may ultimately fail or introduce systematic bias when presented with real scanner data if certain acquisition or object features are discounted or overlooked. A comprehensive account of all MR parameters and appurtenances within a reconstruction framework is by no means trivial [eg, see (19–22)], yet the use of a haptic phantom counterpart may facilitate identification of the most salient factors. In many cases, such elements may even be incorporated into the analytical signal model, allowing more complex and sophisticated simulations. Nevertheless, although we have catalogued the existence of analytical Fourier expressions for a variety of objects, introducing additional experimental factors—especially those such as arbitrary field perturbations—may lead to mathematically intractable situations. Conversely, scanner hardware imperfections or patient-induced perturbations may be difficult to identify or characterize without knowledge of the ideal or unperturbed signal. Clearly, a more synergistic approach would serve as a preferred benchmark for MR reconstruction validation. 3D printing could, therefore, serve as an effective bridge, whereby 3D models typifying specific anatomical structures could be quickly and easily generated, facilitating a robust evaluation of reconstruction performance in common clinical applications.

The medical field has already embraced 3D printing as a promising tool, with applications in surgical planning, prosthetics, and tissue engineering, often relying upon imaging data for modeling patient-specific anatomical features [for reviews, see (23,24)]. Alternatively, we here introduce the converse, using 3D printing for validating and characterizing new imaging approaches. Although the requirement for a haptic counterpart to a numerical design would somewhat undermine the flexibility afforded by strictly numerical testing—necessitating an archetypal phantom corresponding to the investigated anatomical or geometrical object type—this limitation may be counterbalanced by the steadily decreasing associated costs, reduced printing times, and the open-source prospects occasioned by rapid prototyping. One can therefore envision entire publicly accessible databases, whereby a suitable phantom design could be downloaded, modified, and printed for a particular setting. Though it is certainly true that differences exist among 3D printing platforms and manufacturers, these inherent variations may produce negligible effects for a wide variety of applications.

CONCLUSION

In this study, we have demonstrated the efficacy of 3D printing as a means for actualizing a class of models for which analytical Fourier transforms are available for both the full 3D object and its projection onto a finite slice thickness. As proof of concept, we developed a novel Shepp-Logan type phantom that offers a more suitable means of evaluating the spatial characteristics of a given MRSI reconstruction strategy. We further propose a more unified framework for the evaluation and validation of novel model-based MR reconstruction strategies, founded in the assimilation of numerical and haptic phantom testing as afforded by rapid prototyping.

ACKNOWLEDGMENTS

We thank Antonio Nastasi (University Hospital of Geneva Visceral Surgery and Transplantation Service) and Mitch Heynick (EPFL School of Architecture, Civil and Environmental Engineering [ENAC] Output Center and 3D Prototyping Laboratory) for helpful discussions concerning the phantom design and the rapid prototyping process. We also thank Ksenya Shchors (Swiss Institute for Experimental Cancer Research [ISREC]) for assistance in preparing the various phantom solutions.

REFERENCES

1. Grimm T. User's guide to rapid prototyping. Society of Manufacturing Engineers; 2004.
2. Phantom Test Guidance for the ACR MRI Accreditation Program. http://www.acr.org/~/media/ACR/Documents/Accreditation/MRI/LargePhantomGuidance.pdf%3E. Published July 16, 2006. Updated October 24, 2008. Accessed July 15, 2014.
3. Gunter JL, Bernstein MA, Borowski BJ, Ward CP, Britson PJ, Felmlee JP, Schuff N, Weiner M, Jack CR. Measurement of MRI scanner performance with the ADNI phantom. Med Phys 2009;36:2193–2205.
4. Wang D, Doddrell DM, Cowin G. A novel phantom and method for comprehensive 3-dimensional measurement and correction of geometric distortion in magnetic resonance imaging. Magn Reson Imaging 2004;22:529–542.
5. O'Callaghan J, Wells J, Richardson S, Holmes H, Yu Y, Walker-Samuel S, Siow B, Lythgoe MF. Is your system calibrated? MRI gradient system calibration for pre-clinical, high-resolution imaging. PLoS One 2014;9:e96568.
6. Woo DC, Kim BS, Jung SL, Park HJ, Rhim HS, Jahng GH, Choe BY. Development of a cone-shape phantom for multi-voxel MR spectroscopy. J Neurosci Methods 2007;162:101–107.
7. Shepp LA, Logan BF. The Fourier reconstruction of a head section. IEEE Trans Nucl Sci 1974;21:21–43.
8. Koay CG, Sarlls JE, Ozarslan E. Three-dimensional analytical magnetic resonance imaging phantom in the Fourier domain. Magn Reson Med 2007;58:430–436.
9. Greengard L, Stucchio C. Spectral edge detection in two dimensions using wavefronts. Appl Comput Harm Anal 2011;30:69–95.
10. McInturff K, Simon PS. The Fourier transform of linearly varying functions with polygonal support. IEEE Trans Antennas Propag 1991; 39:1441–1443.
11. Ngo T, Fung G, Tsui B, McVeigh E, Herzka D. Three Dimensional Digital Polyhedral Phantom Framework with Analytical Fourier Transform and Applications in Cardiac Imaging. In Proceedings of the 19th Annual Meeting of ISMRM, Montréal, Québec, Canada, 2011. p 1310.
12. Komrska J. Algebraic expressions of shape amplitudes of polygons and polyhedra. Optik 1988;80:171–183.
13. Guerquin-Kern M, Lejeune L, Pruessmann KP, Unser M. Realistic analytical phantoms for parallel magnetic resonance imaging. IEEE Trans Med Imaging 2012;31:626–636.
14. Komrska J. Simple derivation of formulas for Fraunhofer diffraction at polygonal apertures. J Opt Soc Am 1982;72:1382–1384.
15. Barkhuijsen H, de Beer R, van Ormondt D. Improved algorithm for noniterative time-domain model fitting to exponentially damped magnetic resonance signals. J Magn Reson 1987;73:553–557.
16. Haacke EM. Magnetic resonance imaging physical principles and sequence design. New York, NY: Wiley-Liss; 1999.
17. Lustig M, Donoho DL, Santos JM, Pauly JM. Compressed Sensing MRI. IEEE Signal Process Mag 2008;25:72–82.
18. Pruessmann KP, Weiger M, Scheidegger MB, Boesiger P. SENSE: sensitivity encoding for fast MRI. Magn Reson Med 1999;42:952–962.
19. Fessler JA. Model-based image reconstruction for MRI. IEEE Signal Process Mag 2010;27:81–89.
20. Liang ZP, Boada F, Constable R, Haacke EM, Lauterbur P, Smith MR. Constrained reconstruction methods in MR imaging. Reviews of Magnetic Resonance in Medicine 1992;4:67–185.
21. Tsao J, Boesiger P, Pruessmann KP. k-t BLAST and k-t SENSE: dynamic MRI with high frame rate exploiting spatiotemporal correlations. Magn Reson Med 2003;50:1031–1042.
22. Kasten J, Lazeyras F, Van De Ville D. Data-driven MRSI spectral localization via low-rank component analysis. IEEE Trans Med Imaging 2013;32:1853–1863.
23. Rengier F, Mehndiratta A, von Tengg-Kobligk H, Zechmann CM, Unterhinninghofen R, Kauczor HU, Giesel FL. 3D printing based on imaging data: review of medical applications. Int J Comput Assist Radiol Surg 2010;5:335–341.
24. Giannatsis J, Dedoussis V. Additive fabrication technologies applied to medicine and health care: a review. Int J Adv Manuf Technol 2009;40:116–127.

SUPPORTING INFORMATION

Additional Supporting Information may be found in the online version of this article.

Supporting Figure S1. Sample line profile plots for the slice portrayed in the rightmost column of Figure 3. RMSE values are given for both the rasterized and analytical reconstructions in reference to the measured data. The deviations of the measured data when compared with the rasterized and analytical reconstructions also indicate the presence of an inhomogeneous B_1 field, which is not accounted for in the simulation process.

Supporting Table S1. ABS Material Properties